Polymer Testing 155 (2026) 109093

Contents lists available at ScienceDirect

Polymer Testing

journal homepage: www.elsevier.com/locate/polytest

High-throughput micro-indentation method for temperature-dependent static and dynamic characterization of structural adhesives

Chao Kang [a,b,*], Yoichi Okamoto [c], Ming Ji [b], Keiyu Ikeda [c], Yu Sekiguchi [b], Masanobu Naito [d], Chiaki Sato [b]

[a] College of Mechanical Engineering, Zhejiang University of Technology, Hangzhou, China
[b] Laboratory for Future Interdisciplinary Research of Science and Technology, Institute of Integrated Research, Institute of Science Tokyo, Yokohama, Japan
[c] Department of Mechanical Engineering, Institute of Science Tokyo, Yokohama, Japan
[d] Research Center for Macromolecules and Biomaterials, National Institute for Materials Science (NIMS), 1-2-1 Sengen, Tsukuba, Ibaraki, 305-0047, Japan

ARTICLE INFO

Keywords:
Indentation
High-throughput
Polymer mechanics
Viscoelasticity
Dynamic mechanical analysis
Materials informatics

ABSTRACT

Characterizing the temperature-dependent mechanical properties of structural adhesives is critical for industrial applications in aerospace, automotive, and electronics. The increasing integration of artificial intelligence (AI) in material discovery has amplified the demand for large, high-quality datasets, which conventional mechanical testing methods often cannot efficiently provide. In this study, a novel micro-indentation method is introduced that enables rapid and accurate evaluation of static and dynamic mechanical properties of structural adhesives across a wide temperature range. A 3-mm spherical indenter is utilized to perform both quasi-static and dynamic loading on flat bulk samples, enabling accurate multi-modal measurement through independent and precise temperature control of both the indenter and the bulk material, thereby ensuring reliable measurements with minimal sample preparation. Static indentation tests on epoxy and acrylic samples demonstrated that the elastic modulus can be accurately obtained from unloading data, even with plastic deformation, using the Oliver–Pharr method. Dynamic testing further revealed that the epoxy exhibited higher storage and loss moduli than the acrylic adhesive, indicating superior mechanical performance at elevated temperatures. Conversely, the acrylic adhesive exhibited a lower glass transition temperature, indicating a narrower operational temperature range, and a higher loss factor, reflecting greater energy dissipation. The proposed method enhances the efficiency and accuracy of mechanical characterization, enabling the high-throughput testing necessary to generate datasets for AI-driven material development. By enabling rapid design and optimization of polymers, this technique is promising for advancing material discovery with tailored properties.

1. Introduction

The accelerating pace of material discovery and optimization increasingly relies on the synergy between advanced computational methods and experimental science. Machine learning (ML) has emerged as central to this paradigm, enabling the analysis of large datasets to predict and design new materials with high accuracy [1–3]. The performance of ML models depends on the availability of large, high-quality training datasets [4]. In materials science, this has created a strong demand for high-throughput experimental techniques capable of rapidly generating datasets on key material properties such as hardness, elastic modulus, and fracture toughness [5–8]. Integrating such techniques with data science has revolutionized the material development cycle, enabling iterative, feedback-driven processes that have advanced the discovery of new alloys [9], composites [10], and polymeric materials [11,12].

Characterizing the intrinsic mechanical response of polymeric materials is critical for their use in industries such as aerospace [13], automotive [14], and electronics [15]. Their behavior is highly sensitive to operational conditions, notably temperature and loading [16–18]. Consequently, a comprehensive understanding requires evaluation of static and dynamic properties, as polymers exhibit complex temperature-dependent responses ranging from elastic to viscoelastic and plastic. For accurate performance prediction and optimization, particularly under time-dependent or cyclic loading, accurate measurements of static properties (elastic modulus) and dynamic properties

* Corresponding author. College of Mechanical Engineering, Zhejiang University of Technology, Hangzhou, China.
E-mail address: kangchao@zjut.edu.cn (C. Kang).

https://doi.org/10.1016/j.polymertesting.2026.109093
Received 18 October 2025; Received in revised form 4 December 2025; Accepted 8 January 2026
Available online 8 January 2026

(creep, stress relaxation, and complex modulus) are necessary.

Conventional bulk-scale mechanical tests, such as tensile and compression tests, are crucial to material characterization. However, they are inefficient, require large, specially prepared samples, and are often inadequate for probing localized or time-dependent behavior. These limitations have driven the adoption of localized techniques, with nanoindentation emerging as a prominent method for high-resolution measurements of mechanical properties at the nanoscale [19]. Nanoindentation is widely applied for static and dynamic characterization, enabling the evaluation of hardness, elastic modulus, and creep in thin films, coatings, and limited material volumes [20–24]. Its dynamic variant, using cyclic loading or continuous stiffness measurements, further allows the analysis of viscoelastic and fatigue properties [25,26], making nanoindentation a versatile tool across diverse material systems [27,28].

Despite its versatility, nanoindentation faces numerous limitations that impede its broad application, particularly for high-throughput testing of soft materials. A major challenge includes accurately determining the projected contact area between the indenter and sample [29–31]. This issue is pronounced in soft, viscoelastic polymers, which undergo considerable deformation, including pile-up or sink-in around the indenter, resulting in errors in contact area estimation and property calculations. Furthermore, its efficiency in high-throughput testing is hampered by the demanding sample preparation, as surfaces must be extremely flat and polished to ensure measurement accuracy [32]. Consequently, nanoindentation is less suitable for rapid, precise measurements across varying conditions, specifically when temperature is a key factor.

This study presents the development and thorough validation of a novel micro-indentation device designed for the high-throughput characterization of structural adhesives. This system employs a 3-mm spherical indenter and features independent, precise temperature control, enabling accurate multi-modal measurement across a wide thermal range. The indentation depth used in this study is typically in the order of dozens of micrometers, classifying the method within the micro-indentation regime, which is larger than conventional nano-indentation depths and well below the macro-scale. This significantly simplifies sample preparation compared to nano-indentation and improves contact-area determination, thus streamlining the measurement process. Validation was rigorously performed via a direct comparison of dynamic properties with those obtained from a commercial rheometer, confirming the device's reliability. This work establishes critical insights into the relationship between indentation depth, material composition, and temperature on mechanical property measurement. Ultimately, the high efficiency and multi-modal data generation capability of this system directly support the demand for large, high-quality datasets necessary for machine-learning-driven material design.

2. Experimental

2.1. Setup

The custom-developed micro-indentation testing device for efficient mechanical characterization of structural adhesives is illustrated in Fig. 1. The system comprises three primary modules: driving and supporting, data acquisition, and temperature control. Indentation tests were conducted using a 3.0-mm-diameter spherical indenter, whose vertical motion was controlled to apply predefined loading conditions. The 3.0-mm indenter provided the optimal contact area for the materials analyzed in this work. For applications involving different materials, the indenter geometry and size must be appropriately adapted. Displacement and force at the contact point were measured using a linear variable differential transformer (LVDT) and a piezoelectric force sensor, respectively. Independent heating and cooling systems allowed precise temperature control of the sample and indenter.

The vertical motion of the indenter was driven by a voice coil motor (VCM, X-2606, NEOMAX, Japan), the key component of the driving and supporting module. The VCM comprises a fixed magnet and coil mounted on a vertical linear guide, enabling precise displacement. A spring assists coil movement, while the applied current generates a magnetic force that drives the coil and indenter, ensuring accurate control of loading rate and frequency. The indenter and connecting rod were fabricated using SUS304 steel, selected for its low thermal conductivity and nonmagnetic properties.

The temperature control module ensured stable thermal conditions for the indenter and sample. The indenter temperature was regulated by a heater mounted above it, with epoxy adhesive applied to enhance thermal transfer. A thermocouple bonded near the indenter tip enabled direct temperature monitoring. To prevent thermal drift and overheating of upper components, particularly the load cell, cooling water was circulated through an aluminum container mounted above the indenter. The sample was positioned on a bronze heater, and its temperature was monitored using a thermocouple attached near the indentation point. A proportional-integral-derivative (PID) control system maintained the target temperatures of the indenter and sample throughout testing.

The data acquisition module recorded real-time displacement and force data with high precision. An LVDT installed at the top of the indenter rod measured vertical displacement. Frame compliance, a critical factor for accurate displacement calculations, was calibrated as

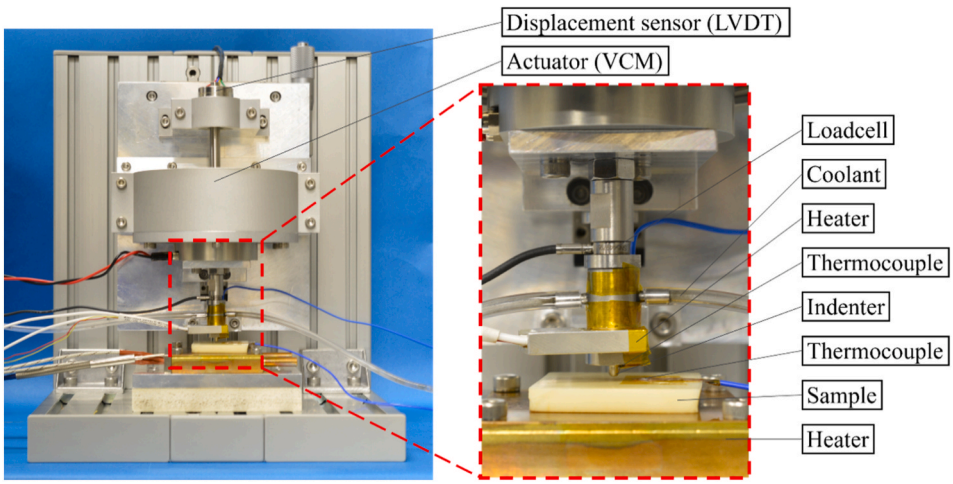

Fig. 1. Photographs of the custom-built micro-indentation setup, showing the driving and supporting, data acquisition, and temperature control modules.

discussed in Section 4.1.2. A flat piezoelectric ring-force sensor (9130C, Kistler, Switzerland) positioned above the cooling components measured the applied compression force. The entire system was automated using a custom-written LabVIEW program, with data collected using a National instrument data acquisition (DAQ) device (PCIe-6314).

2.2. Testing samples

2.2.1. Materials

Two thermoset structural adhesives were selected for testing: a one-component epoxy adhesive (Cemedine Co., Ltd., Tokyo, Japan) and a two-component second-generation acrylic (SGA) adhesive, Hardloc C355-20 (Denka Corp., Tokyo, Japan). The epoxy adhesive, comprising primarily a bisphenol A epoxy base resin with dicyandiamide (DICY) as the curing agent, was cured at 180 °C for 60 min. Carboxyl-terminated butadiene acrylonitrile (CTBN) rubber was incorporated to improve fracture toughness. The acrylic adhesive was cured at approximately 24 °C for 24 h, followed by post-curing at 60 °C for 2 h. Epoxy and acrylic materials were selected as the testing materials because of their wide application in structural adhesives.

Baseline mechanical properties of both adhesives were obtained from tensile tests on standard flat dog-bone specimens (Fig. 2) [33,34]. The tensile tests for both materials were conducted at room temperature using a universal testing machine (AUTOGRAPH, Shimadzu Corporation, Kyoto, Japan). The epoxy sample had a thickness of 2.9 mm and a cross-section of 5 × 7 mm^2, while the acrylic sample had a thickness of 3.0 mm and a cross-section of 6 × 33 mm^2. The epoxy exhibited a brittle response with elastic behavior during initial loading, while the acrylic showed ductile behavior with inelastic strain throughout its loading history. Poisson's ratios (ν) were measured as 0.41 and 0.37 for the epoxy and acrylic adhesives, respectively. Tests were conducted at displacement rates of 1 and 5 mm/min for epoxy and acrylic, respectively.

2.2.2. Sample preparation

Flat block samples (40 × 40 mm^2, 6 mm thickness) were prepared for indentation tests following the method of Lucus [35], originally described in French patent NF T 76–142 [36]. For the two-component adhesive, the mixture was poured into a stainless-steel mold (Fig. 3) [37], with a silicone rubber frame used to control sample dimensions. The frame was secured by an external metallic frame, and a metal lid was placed on top before applying a pressure of 2 MPa using a hot press. Curing under pressure prevented air entrapment and void formation. Samples were demolded after cooling to room temperature.

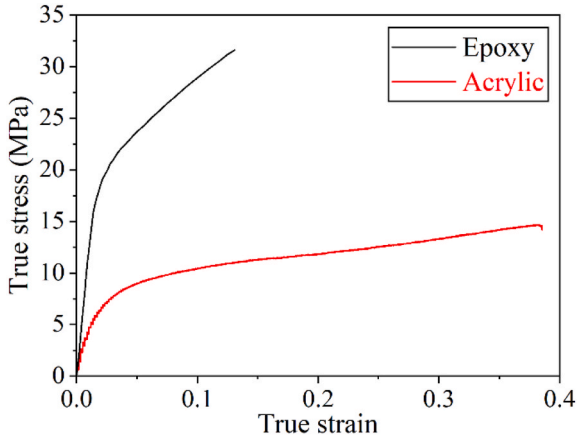

Fig. 2. Stress-strain curves of the one-component epoxy and two-component acrylic adhesives using static tensile tests.

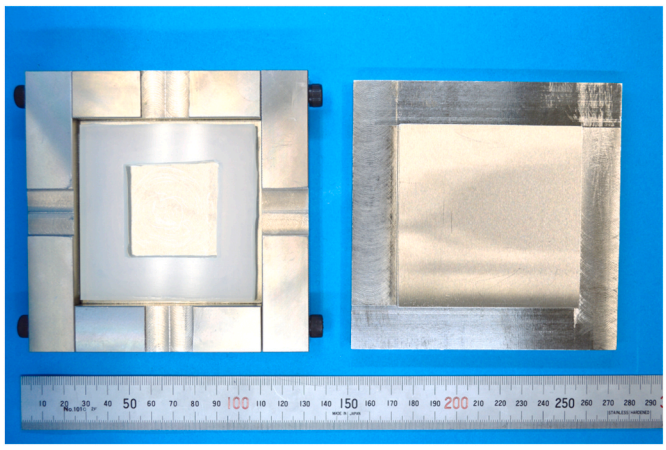

Fig. 3. Stainless-steel mold used for fabricating the flat block indentation samples.

2.3. Test conditions

Both static and dynamic tests were conducted under force control, with the indentation force precisely regulated via the input voltage applied to the VCM actuator. The input voltage profiles for static and dynamic tests are shown in Fig. 4. In static tests, the loading and unloading times were 4 s for the epoxy and 2 s for the acrylic, with a 1 s hold before unloading. Dynamic tests included a 3 s loading period, 1 s holding, and 25 s of cyclic loading at 1 Hz. To establish firm contact

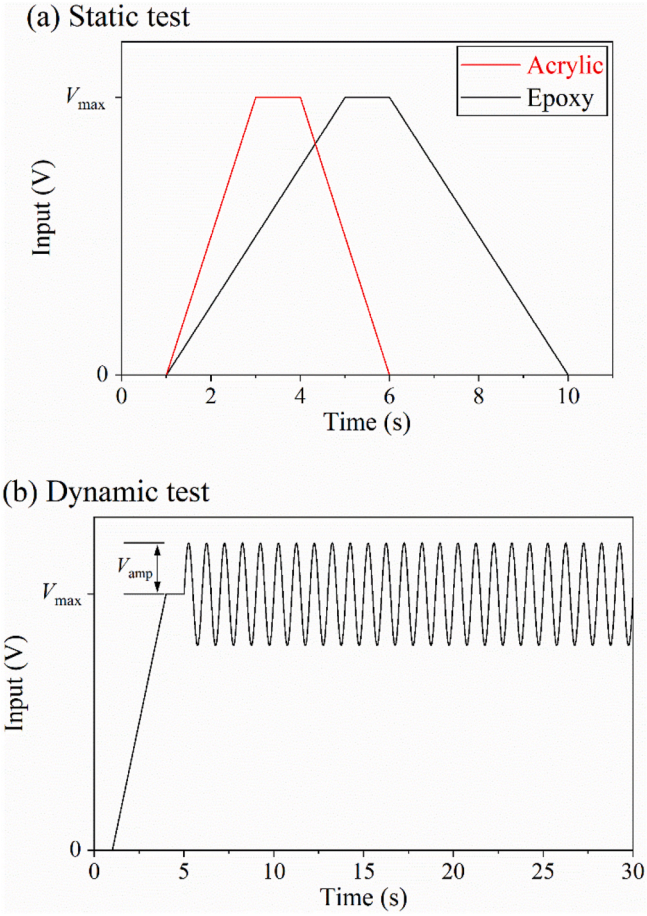

Fig. 4. Schematic of the loading conditions for (a) static and (b) dynamic indentation tests.

prior to indentation tests, the indenter was moved downward to contact the sample surface, and a pre-load of approximately 0.1 N was applied.

Typical voltages, including maximum load, offset, and amplitude, were selected based on material type and test temperatures. The detailed loading conditions for static and dynamic tests are presented in Tables 1 and 2, respectively.

3. Theory and calculations

The elastic and dynamic moduli of the samples were derived from the displacement and force responses measured during micro-indentation. As illustrated in Fig. 5, indentation was performed on viscoelastic sample using a spherical indenter. As the indentation depth and contact area are considerably smaller than the sample dimensions, the sample can be treated as a semi-infinite block, a key assumption in indentation theory. The reduced modulus E_r is expressed as follows [38]:

$$E_r = \frac{\sqrt{\pi}}{2\sqrt{A}} S, \tag{1}$$

where E_r includes the elastic response of both the sample and the indenter tip. S represents the contact stiffness between the indenter tip and sample surface and A the projected contact area. For a spherical indenter, the projected area is expressed by Eq. (2) when the contact depth h_c is considerably smaller than the indenter radius R_0.

$$A = 2\pi R_0 h_c. \tag{2}$$

Contrary to nanoindentation, which often requires complex empirical corrections for imperfect indenter geometry [39], the large deformation and indenter radius in this study allow for the direct use of Eq. (2) to determine the contact area. Considering indenter deformation, the relationship between the reduced modulus and elastic moduli of the sample and indenter is expressed as follows.

$$\frac{1}{E_r} = \frac{1-\nu_s{}^2}{E_s} + \frac{1-\nu_i{}^2}{E_i}, \tag{3}$$

where E_s and E_i represent the elastic moduli, and ν_s and ν_i the Poisson's ratios of the sample and indenter, respectively. Accurate calculation of the elastic modulus of a sample requires precise measurement of the contact stiffness S and indentation depth h_c. The methodology depends on the deformation type (elastic or inelastic) and loading conditions (static or dynamic).

3.1. Static tests

For purely elastic indentation, the elastic modulus can be directly obtained from the elastic solution [40]:

$$E_r = \frac{3}{4\sqrt{R_0}} \frac{dP}{dh^{1.5}}. \tag{4}$$

The slope of the P-$h^{3/2}$ plot was determined by fitting the displacement-force loading curves, where h represents the total indentation displacement $h = 2h_c$. Indentation data were analyzed using the widely accepted Oliver and Pharr (O–P) method [41], which assumes no plastic deformation during unloading. The unloading data were fitted to the following power-law expression as follows:

$$P = B\left(h - h_f\right)^m, \tag{5}$$

Table 1
Summary of the loading conditions for the static indentation tests.

	V_{max} (V)	P_{max} (N)
Epoxy	0.1–4	0.38–20.4
Acrylic	0.1–1.8	0.44–9.19

where B, h_f, and m represent the fitting parameters. The contact stiffness S at peak load was obtained as the derivative of the unloading curve at maximum displacement h_{max}.

$$S = \frac{dP}{dh}\Big|_{h=h_{max}} = Bm\left(h_{max} - h_f\right)^{m-1}. \tag{6}$$

The contact depth h_c was then calculated from S and peak load P_{max} as follows:

$$h_c = h_{max} - \beta \frac{P_{max}}{S}. \tag{7}$$

The geometric parameter β represents a constant dependent on the indenter shape and equals 0.75 for a spherical indenter [42]. The elastic modulus was then calculated using the h_c and S expressed in Eqs. (1)–(3).

3.2. Dynamic tests

Viscoelastic behavior is represented using a spring-dashpot model. In this study, the Voigt model (which places these elements in parallel) was employed to describe viscoelastic solids [43]. The complex modulus, E^*, is composed of a real part, the storage modulus (E'), and an imaginary part, the loss modulus (E''):

$$E^* = E' + iE''. \tag{8}$$

Storage modulus represents the capacity of a material to store elastic energy, while loss modulus represents its capacity to dissipate energy as heat. Under dynamic sinusoidal loading at frequency ω, the reduced storage modulus (E_r') and reduced loss modulus (E_r'') are expressed as follows:

$$E_r{}' = \frac{\sqrt{\pi}}{2\sqrt{A}} S_c. \tag{9}$$

$$E_r{}'' = \frac{\sqrt{\pi}}{2\sqrt{A}} \omega D_c. \tag{10}$$

The loss factor, tan φ, which is a measure of a material's damping ability, is the ratio of the loss modulus to the storage modulus:

$$\tan\varphi = \frac{E_r''}{E_r'}, \tag{11}$$

where S_c and D_c represent the contact stiffness and damping factors, respectively, derived from the amplitudes of the dynamic force (ΔP_0) and displacement (ΔH_0) and the phase delay (φ) as follows:

$$S_c = \frac{\Delta P_0}{\Delta H_0} \cos\varphi, \tag{12}$$

$$\omega D_c = \frac{\Delta P_0}{\Delta H_0} \sin\varphi. \tag{13}$$

The projected contact area is then determined by substituting Eq. (7) into Eq. (2):

$$A = 2\pi R_0 \left(h_{max} - \beta \frac{P_{max}}{S_c}\right), \tag{14}$$

where S_c is expressed by Eq. l2.

The values of ΔP_0, ΔH_0, and φ were calculated from measured force and displacement signals using a lock-in amplifier [44], which includes two multipliers and low-pass filters (Fig. 6). The measured signal v_{sig} is multiplied by two quadrature reference signals $v_{ref}^{0^\circ}$ and $v_{ref}^{90^\circ}$, expressed as follows:

$$v_{sig}(t) = V_{sig} \cdot \sin\left(\omega_{sig} t + \psi\right), \tag{15}$$

$$v_{ref}^{0^\circ}(t) = V_{ref} \cdot \sin\left(\omega_{ref} t\right), \tag{16}$$

Table 2
Loading conditions for the dynamic indentation tests, where V_{max} and V_{amp} represent the maximum and amplitude voltages of the applied signal, respectively (unit: V).

Temperature (°C)	20–40	45–90	90–100	100–120	125–130	135–170
Epoxy, $V_{max} \pm V_{amp}$	0.4 ± 0.08	0.4 ± 0.08	0.4 ± 0.08	0.3 ± 0.06	0.2 ± 0.04	0.1 ± 0.02
Acrylic, $V_{max} \pm V_{amp}$	0.15 ± 0.03	0.05 ± 0.01	–	–	–	–

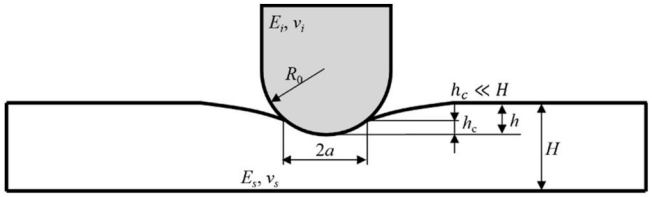

Fig. 5. Schematic of a spherical indenter contacting a semi-infinite surface (not to scale).

$$v_{ref}^{90^\circ}(t) = V_{ref} \cdot \cos(\omega_{ref} t), \tag{17}$$

where v_{sig} and v_{ref} represent amplitudes of the measured and reference signals, respectively, while ω_{sig} and ω_{ref} are the corresponding frequencies, and ψ is the measured signal phase. The multiplier outputs are expressed as follows:

$$v_{sig}(t) \cdot v_{ref}^{0^\circ}(t) = \frac{V_{sig} \cdot V_{ref}}{2} \{\cos[(\omega_{sig} - \omega_{ref})t + \psi] - \cos[(\omega_{sig} + \omega_{ref})t + \psi]\}, \tag{18}$$

$$v_{sig}(t) \cdot v_{ref}^{90^\circ}(t) = \frac{V_{sig} \cdot V_{ref}}{2} \{\sin[(\omega_{sig} - \omega_{ref})t + \psi] + \sin[(\omega_{sig} + \omega_{ref})t + \psi]\}. \tag{19}$$

Subsequently, the dynamic components are filtered through a low-pass filter. For the case where $\omega_{sig} = \omega_{ref}$, the outputs are:

$$X = \frac{V_{sig} \cdot V_{ref}}{2} \cos\varphi, \tag{20}$$

$$Y = \frac{V_{sig} \cdot V_{ref}}{2} \sin\varphi. \tag{21}$$

From the aforementioned, the amplitude and phase of the measured signal are derived as follows:

$$V_{sig} = \frac{2}{V_{ref}} \sqrt{X^2 + Y^2}, \tag{22}$$

$$\varphi = \tan^{-1}\frac{Y}{X}. \tag{23}$$

These lock-in amplifier calculations were integrated into the LabVIEW code, enabling direct determination of ΔP_0, ΔH_0, and φ. From these parameters, the dynamic properties (E', E'', and tan φ) were obtained.

4. Results and discussions

4.1. Device calibrations

4.1.1. Dynamic calibration

The dynamic behavior of the indentation system is illustrated in Fig. 7. The total impedance comprises tip–sample contact stiffness (S_c), tip–sample damping factor (D_c), and the mechanical impedance of the instrument (S_{instr} and D_{instr}). The frame stiffness is denoted as S_f, while m represents the equivalent indenter mass. A similar dynamic model has been reported in several studies [45–48]. The governing equations for dynamic indentation, considering these factors, are expressed as follows.

$$\left(\frac{1}{S_c} + \frac{1}{S_f}\right)^{-1} = \frac{\Delta P_0}{\Delta H_0}\cos\varphi + m\omega^2 - S_{instr}, \tag{24}$$

$$\omega D_c = \frac{\Delta P_0}{\Delta H_0}\sin\varphi - \omega D_{instr}. \tag{25}$$

Accurate measurements require prior calibration of S_{instr}, D_{instr}, and S_f. Instrument impedance was calibrated by conducting dynamic tests using a free-hanging indenter (i.e., with no sample). Under these conditions, Eqs. (24) and (25) can be simplified as follows:

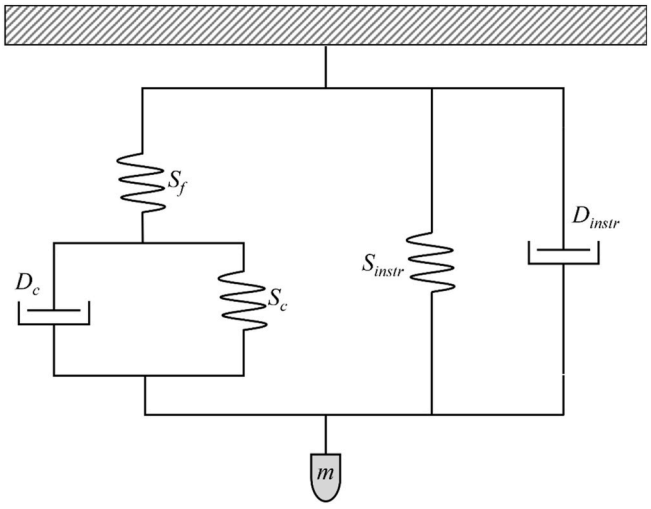

Fig. 7. Schematic of the dynamic model of the indentation system, incorporating a parallel spring-dashpot element (Voigt model) to capture the viscoelastic response of the sample.

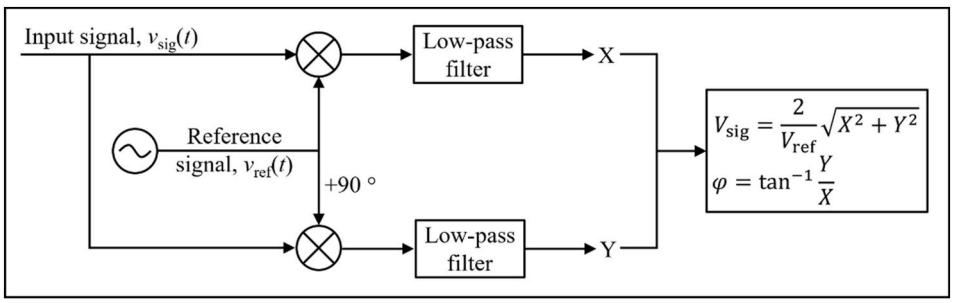

Fig. 6. Schematic of a lock-in amplifier used to derive the amplitude and phase of the measured signals.

$$S_{instr} - m\omega^2 = \frac{\Delta P_0}{\Delta H_0}\cos\varphi|_{\text{free-hanging}}, \tag{26}$$

$$\omega D_{instr} = \frac{\Delta P_0}{\Delta H_0}\sin\varphi|_{\text{free-hanging}}. \tag{27}$$

Averaged results from 10 free-hanging tests at 1 Hz yielded $S_{instr}-m\omega^2$ = 23.6 N/m and ωD_{instr} = 22.4 N/m. These results confirm that instrument impedance is limited by frame stiffness and sample impedance.

4.1.2. Static calibration

The frame compliance C_f (representing rod frame deformation) was calibrated via static indentation tests using a fused silica reference sample [49]. Preliminary results confirmed that frame stiffness S_f was several orders of magnitude higher than the instrument impedance S_{instr}, making it the dominant contributor to the overall system compliance. The mechanical model of the static indentation system is illustrated in Fig. 8, where the total system compliance C_{total} represents the sum of the frame compliance and contact compliance C_c.

$$C_{total} = C_f + C_c. \tag{28}$$

As expressed in Eq. (1), the contact compliance is as follows:

$$C_c = \frac{1}{S_c} = \frac{\sqrt{\pi}}{2E_r}\frac{1}{\sqrt{A}}. \tag{29}$$

Substituting Eq. (29) into Eq. (28) results in.

$$C_{total} = C_f + \frac{1}{\sqrt{A}}\frac{\sqrt{\pi}}{2E_r}. \tag{30}$$

Plotting C_{total} against $1/\sqrt{A}$ yields a straight line, where the y-intercept corresponds to the frame compliance C_f. To obtain this plot, numerous indentations were performed on fused silica at varying maximum forces. The total compliance, $C_{total} = 1/S_{total}$, was derived from unloading curves using the Oliver–Pharr method (Eqs. (5)–(7)). The projected contact area A was calculated by assuming constant hardness H for the fused silica as follows:

$$A = \frac{P_{max}}{H}, \tag{31}$$

where P_{max} represents the maximum load and H is assumed to be 10 GPa [50]. Results from 35 indentations (Fig. 9) confirmed a linear relationship, yielding a frame stiffness, S_f (where $S_f = 1/C_f$), was calculated to be 1.89 × 10^6 N/m.

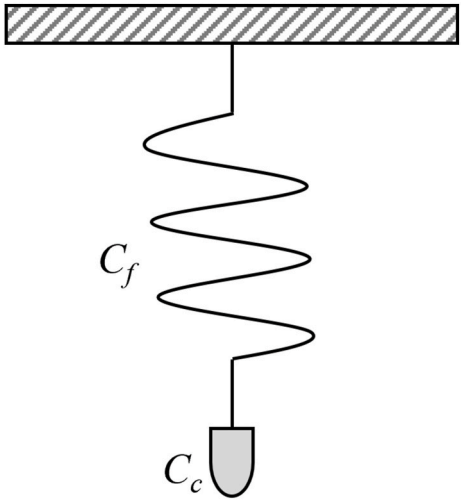

Fig. 8. Schematic of the mechanical model of the static indentation system, developed for frame stiffness calibration.

4.2. Static measurements

4.2.1. Load-displacement curves and elastic modulus

No cracking or fracture occurred in the epoxy or acrylic adhesive samples during indentation; hence, fracture mechanics were not considered. Displacement-force (*h-f*) curves at 20 °C are shown in Fig. 10 for the epoxy (a) and acrylic samples (b) at different maximum loads (F_{max}). In both cases, displacement increased with F_{max}. A slight viscous deformation was observed during the 1-s hold at the peak force.

For epoxy adhesive (Fig. 10a), the unloading and loading curves nearly overlapped with the loading curve when F_{max}<10 N, indicating primarily elastic deformation. At higher F_{max}, inelastic deformation occurs, shifting the unloading curve below the loading curve. This inelastic response, attributable to plastic deformation under increased stress, resulted in a residual displacement of approximately 0.005 mm at F_{max} = 23.5 N. These results indicate that elastic modulus calculations based on loading data are unreliable beyond a critical value.

For the acrylic adhesive (Fig. 10b), inelastic deformation was evident at all F_{max} values. The residual displacement increased with load, indicating greater inelasticity. As confirmed by tensile tests (Fig. 2), the acrylic adhesive deformed viscoplastically from the beginning of loading. Hence, the loading data could not be employed to determine the elastic modulus.

The *h-f* curves of the epoxy adhesive at different temperatures (20, 120, and 150 °C) are shown in Fig. 10c. Both maximum and residual indentation displacements increased with temperature, with a considerable difference between 120 and 150 °C, indicating a critical change in the properties of the material within this range.

4.2.2. Effects of indentation depth, sample materials, and computing methods

The elastic moduli of both adhesives were calculated using two methods: (1) a purely elastic model based on loading data and (2) the Oliver–Pharr method, which incorporates plastic deformation using unloading data. The results are shown in Fig. 11 as a function of the maximum indentation displacement (h_{max}). Red plots represent unloading-based calculations, while black plots represent loading-based results. Approximation curves were added to highlight the depth-dependent trends. For the epoxy adhesive, a greater data scatter was observed compared to the acrylic adhesive, primarily owing to minimal absolute displacements, which increased relative displacement errors.

(a) Indentation depth

For both adhesives, a critical maximum indentation depth,

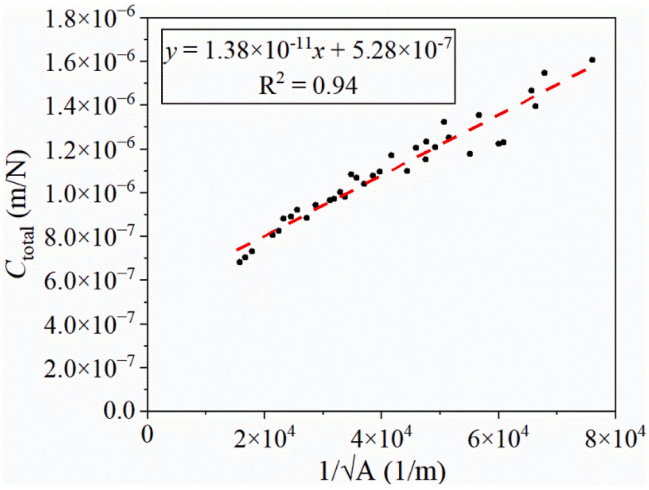

Fig. 9. Graphical determination of frame compliance from indentations on a fused silica under different forces.

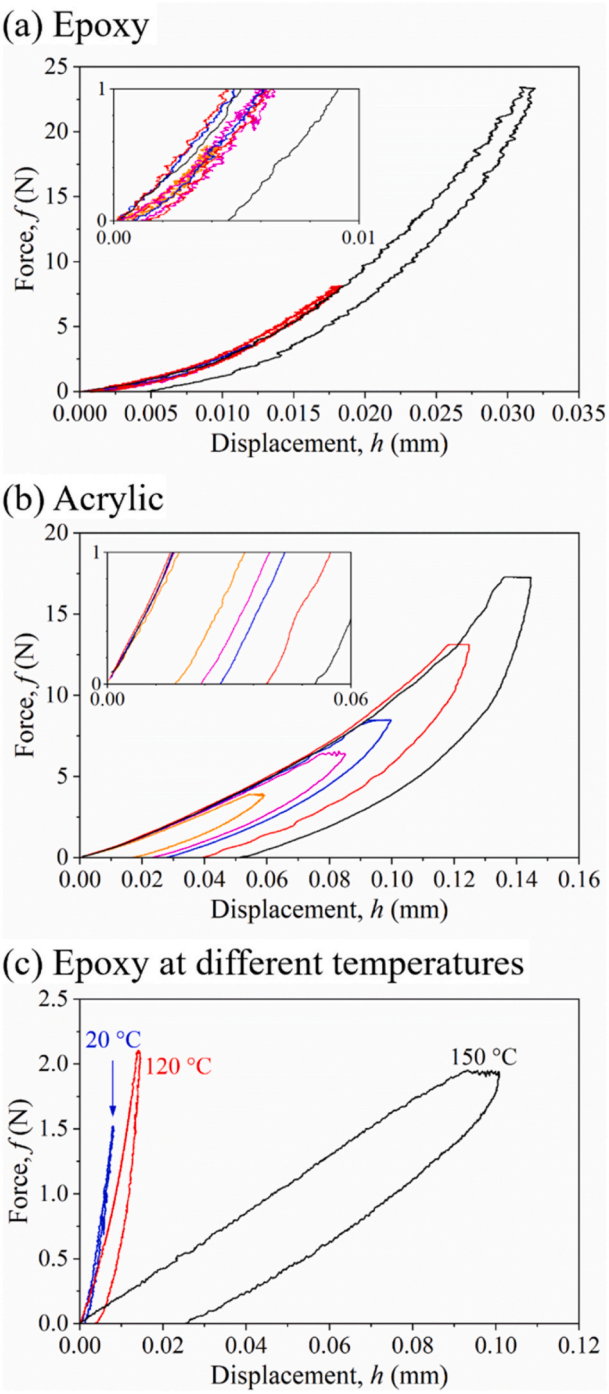

Fig. 10. Displacement-force (*h–f*) curves from static indentation tests for (a) epoxy, (b) acrylic, and (c) epoxy adhesive tested at different temperatures. Insets in (a) and (b) show enlarged low-force regions.

h^c_{max}, was identified. When $h_{max} < h^c_{max}$, the calculated modulus remained constant. Conversely, when $h_{max} > h^c_{max}$, the moduli increased almost linearly with h_{max}. This trend indicates that the semi-infinite assumption holds only when $h_{max} < h^c_{max}$. At greater indentation depths, the stiffer copper contributed to the measurements, artificially elevating the apparent elastic moduli.

The slopes of the fitting curves (dE_s/dh_{max}) for $h_{max} > h^c_{max}$ were calculated using the least-squares method and are presented in Table 3. These slopes quantify the sensitivity of the calculated modulus to indentation depth beyond the critical threshold. For epoxy, the slopes were an order of magnitude higher than those for the acrylic, indicating that the epoxy modulus was greatly influenced by indentation depth in this region. In both materials, dE_s/dh_{max} values derived from loading data were smaller than those from unloading data. This difference was attributed to the underestimation of modulus during loading owing to plastic strain, which was considerable in the ductile acrylic sample. Although the Oliver-Pharr method partially compensates for plastic deformation, viscous effects during unloading can still introduce minor errors in modulus determination.

(b) Sample materials

The h^c_{max} values of the epoxy and acrylic samples were 0.0091 and 0.089 mm, respectively. Normalized by the sample thickness (H = 6 mm), the maximum indentation strains (h^c_{max}/H) were 0.015 % and 0.148 % for epoxy and acrylic, respectively. The epoxy strain was approximately 10 % of that of the acrylic, while the elastic modulus (E_s) was approximately 10 times higher. This inverse relationship between critical indentation depth and elastic modulus indicates that the semi-infinite indentation assumption is satisfied at larger depths in softer materials. While the breakdown of the semi-infinite assumption near sample boundaries is a fundamental principle, this work provides the first quantitative determination of the critical indentation depth (h^c_{max}) using micro-indentation for these adhesive materials. This quantitative finding empirically defines the safe operational limits necessary to ensure the validity of subsequent high-throughput static and dynamic characterization for materials with various mechanical properties.

(c) Computing methods

An elastic modulus of epoxy exhibited a minimal difference between loading and unloading data, while acrylic exhibited a larger discrepancy owing to its pronounced inelastic behavior. In the acrylic, the elastic modulus derived from loading data was considerably lower because plastic deformation during loading reduced the calculated contact stiffness. The steeper slope of the dE_s/dh_{max} plot for unloading data further confirmed this plastic contribution. Although unloading minimizes plastic effects, viscous deformation still influences the unloading curve, introducing inevitable errors in modulus calculation [51].

4.2.3. *Effect of testing temperature*

The temperature effect was examined by indenting the epoxy adhesive at 20, 90, 120, and 150 °C under a consistent peak loading force of approximately 2 N. As shown in the *h-f* curves (Fig. 10c), the indentation was nearly elastic at 20 °C but exhibited considerable viscoplastic deformation at 150 °C. Average elastic moduli from at least five tests, calculated using loading data, are shown in Fig. 12. The modulus decreased approximately linearly from 20 to 120 °C and approached zero at 150 °C, indicating a glass transition temperature between 120 and 150 °C. These results confirm the reliability of the device for high-temperature indentation tests.

4.3. *Dynamic measurements*

Dynamic tests were conducted on epoxy and acrylic samples across a range of temperatures. To ensure the validity of the semi-infinite assumption, maximum indentation displacements were maintained below 0.0091 mm for the epoxy and 0.089 mm for the acrylic, corresponding to peak forces of 2.1 and 6.8 N, respectively. To minimize temperature effects on this assumption, relatively low peak forces were applied at higher test temperatures (Table 2).

4.3.1. *Force and displacement responses*

Force-displacement responses during dynamic testing of epoxy adhesive at 20 °C are shown in Fig. 13a. Detailed responses for the first two cycles at 20 and 145 °C are shown in Fig. 13b and c, respectively. The

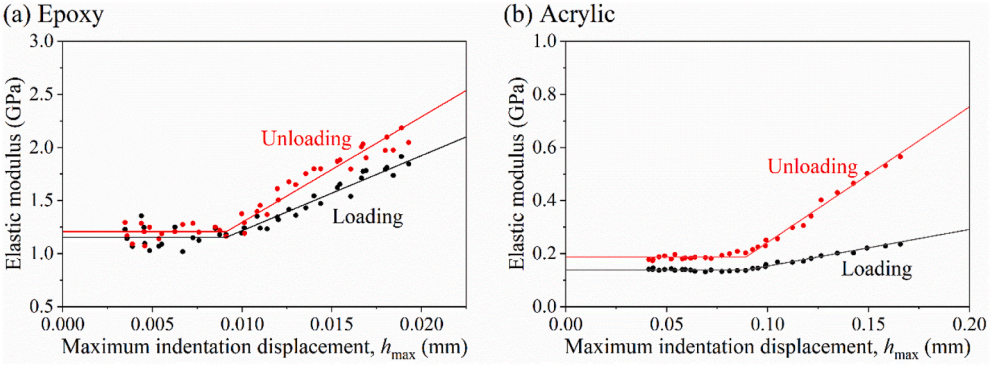

Fig. 11. Elastic moduli of (a) epoxy and (b) acrylic adhesives as a function of maximum indentation depth. The data are derived from the unloading curves (red plots) and loading curves (black plots). Approximation curves illustrate the depth-dependent curves.

Table 3
Summary of maximum indentation depth (h^c_{max}), ratio of maximum depth to hardness (h^c_{max}/H), elastic modulus (E_s), and change rate of modulus variation with depth (dE_s/dh_{max}), as derived from Fig. 11.

	h^c_{max} (mm)	h^c_{max}/H (%)	E_s, GPa	$(dE_s)/(dh_{max})$ (GPa·mm^{-1})
Epoxy-loading data	0.0091	0.015	1.15	70.73
Epoxy-unloading data	0.0091	0.015	1.21	99.51
Acrylic-loading data	0.089	0.148	0.14	1.41
Acrylic-unloading data	0.089	0.148	0.19	5.12

The elastic modulus of the epoxy derived from static indentation (1.1 GPa) corresponded with the tensile test value (1.1 GPa). For the acrylic adhesive, the indentation modulus corresponded with the 2 % or 5 % secant moduli (0.29 and 0.14 GPa, respectively), thereby confirming the reliability of the proposed method for brittle and ductile polymers.

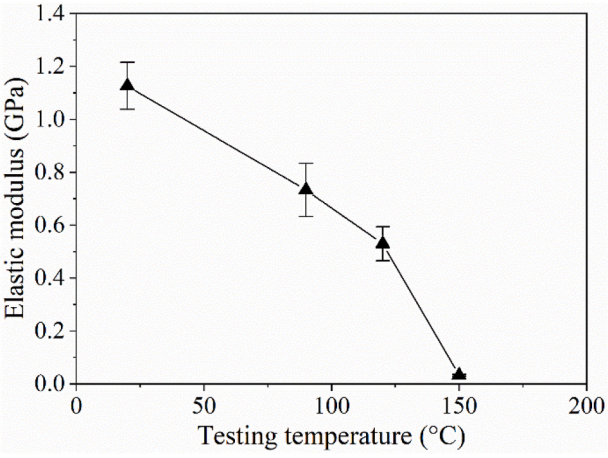

Fig. 12. Elastic modulus of the epoxy adhesive obtained from static indentation tests at different temperatures.

results confirm that cyclic loading signals were accurately reproduced. At elevated temperatures, the displacement exhibited a pronounced phase lag at 145 °C, indicating enhanced viscoelastic behavior.

4.3.2. *Dynamic test results*

The storage modulus (E'), loss modulus (E''), and loss factor (tan φ) of the epoxy and acrylic adhesives were determined at different temperatures. Validation of the developed method is shown in Fig. 14, wherein the temperature-dependent dynamic moduli and loss factors of the epoxy adhesive are compared with those measured using a commercial rheometer (Anton Paar MCR702e). The plots show that the values obtained using the micro-indentation device corresponded with those from the rheometer, wherein the dynamic moduli were calculated using $E = 2G(1+\nu)$, where G and ν represent the shear modulus and Poisson's ratio, respectively. Notably, the glass transition temperature, identified by the peak loss factor, was consistent between both methods. While Fig. 14 confirms the accuracy and reliability of the developed device, the core value of the device lies in the multi-modal capability and its ability to test simply prepared bulk flat samples. This drastically reduced sample preparation effort, combined with validated accuracy, provides the essential efficiency needed for data-intensive material screening and accelerated development.

Fig. 15 compares the dynamic results for the epoxy and acrylic adhesives. The epoxy adhesive was tested across a wide range, up to 170 °C higher than that of the acrylic adhesive whose testing was constrained to the 20 °C–90 °C range because further heating would cause excessive material softening, deformation, or thermal degradation, which exceeds its practical operational limit and violates the test assumptions. Epoxy exhibited higher storage and loss moduli, confirming superior stiffness and damping at elevated temperatures. Contrarily, the acrylic exhibited a higher loss factor, indicating greater energy dissipation. The peak loss factor of the epoxy occurred at approximately 145 °C, considerably above that of the acrylic, highlighting the superior high-temperature performance of epoxy and greater damping and viscous deformation of acrylic.

Overall, although the current indentation device requires further comprehensive validation on the factors such as sample geometry, material anisotropy, and extended testing temperatures, the static and dynamic results validate the reliability of the developed micro-indentation device for evaluating the mechanical properties of bulk structural adhesive materials. While it is primarily for compression, with appropriate corrections for localized inhomogeneities or anisotropy, the technique could be applied to a wider range of continuous solids. The developed device requires only a simple, flat bulk sample, substantially reducing the complex machining and preparation time required for conventional methods such as nano-indentation. Furthermore, the system provides a full temperature-dependent static and dynamic property curve in several hours, offering a critical efficiency advantage over sequential, conventionally-tested samples. With its efficiency in sample preparation and measurement, the device offers a considerable advantage over conventional methods for rapid mechanical property evaluation. This capability is important for generating large, high-quality datasets required for machine-learning models, thereby accelerating material development and advancing mechanical characterization.

5. Conclusions

This study developed and validated an efficient micro-indentation method for evaluating the static and dynamic properties of structural

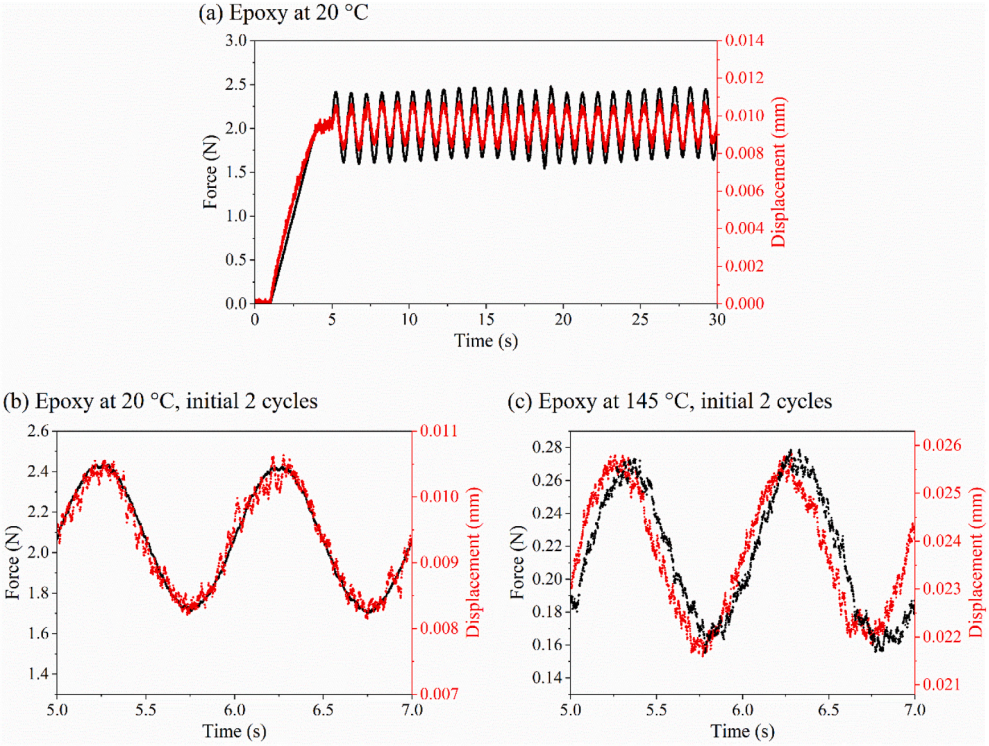

Fig. 13. Force-displacement curves from dynamic tests of the epoxy adhesive at 20 °C. The force and displacement responses for the first two cycles are shown in detail for tests conducted at (a) 20 and (b) 145 °C.

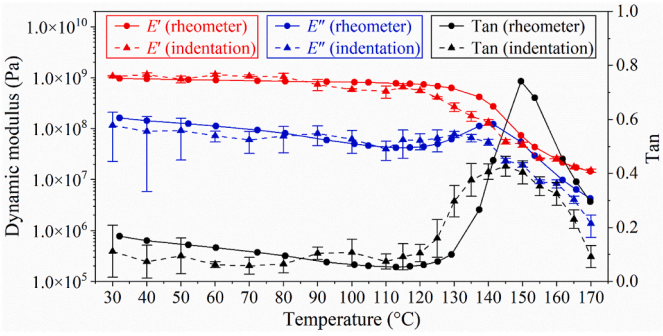

Fig. 14. Storage modulus (E'), loss modulus (E''), and loss factor (tan φ) of the epoxy adhesive as a function of temperature from dynamic micro-indentation at 1 Hz, compared with commercial rheometer results.

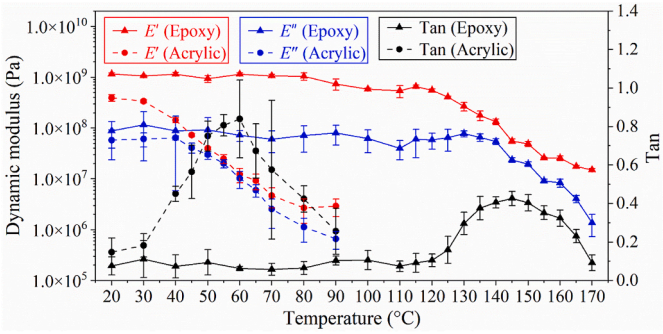

Fig. 15. Comparison of dynamic properties, including storage modulus (E') and loss modulus (E''), of the epoxy and acrylic adhesives as a function of temperature, measured using the proposed device.

adhesives across a wide temperature range. The custom-designed device, incorporating independent temperature control and a theoretical framework, effectively addressed the challenges of rapid and multimodal characterization. The principal contributions are as follows:

- The developed method accurately captures the load-displacement behavior of structural adhesives under static conditions, enabling reliable determination of elastic moduli even in the presence of plastic deformation. It further demonstrates the effects of indentation depth, material composition, computational methods, and testing temperature on static measurements.
- The micro-indentation method reliably captured dynamic viscoelastic properties, with the calculated storage modulus, loss modulus, and loss factor corresponding with those obtained using a commercial rheometer. These temperature-dependent measurements provide valuable insights into material behavior, showing that the epoxy adhesive exhibits considerably higher storage modulus (E') and loss modulus (E') than the acrylic adhesive, while the lower temperature of its peak loss factor (tan φ) indicates a glass transition at an earlier stage.
- The capability of the device to perform accurate measurements at elevated temperatures was validated using two separate temperature control systems for the indenter and sample. These results confirm that the mechanical properties of structural adhesives vary considerably with increasing temperature, particularly near their glass transition temperatures (T_g).

In summary, the proposed micro-indentation method offers a robust and versatile approach for multifunctional mechanical characterization of structural adhesives. Its ability to integrate static and dynamic measurements with high precision across temperatures makes it suitable for rapid material evaluation and development. Although this study focused on two adhesives, the underlying methodology and device principles are broadly applicable to diverse polymeric materials and continuous solids, provided that specific modifications to the indenter tip geometry and

size are implemented to match the material's microstructural features. Future advancements in this technique, including incorporating machine learning for accelerated data analysis, could further accelerate material development cycles.

CRediT authorship contribution statement

Chao Kang: Writing – review & editing, Writing – original draft, Visualization, Software, Methodology, Investigation, Funding acquisition, Formal analysis, Data curation, Conceptualization. **Yoichi Okamoto:** Software, Methodology, Investigation, Formal analysis, Data curation. **Ming Ji:** Methodology, Formal analysis, Data curation, Conceptualization. **Keiyu Ikeda:** Software, Formal analysis, Data curation. **Yu Sekiguchi:** Supervision, Methodology, Formal analysis, Conceptualization. **Masanobu Naito:** Supervision, Project administration, Funding acquisition, Conceptualization. **Chiaki Sato:** Writing – review & editing, Supervision, Software, Project administration, Methodology, Funding acquisition, Data curation.

Declaration of competing interest

The authors declare that they have no known competing financial interests or personal relationships that could have appeared to influence the work reported in this paper.

Acknowledgments

This study was supported by the Core Research for Evolutional Science and Technology (CREST) program “Revolution material development by fusion of strong experiments with theory/data science” of the Japan Science and Technology Agency, Grant JPMJCR19J3. Chao Kang acknowledges support from the National Natural Science Foundation of China (52505162).

Data availability

Data will be made available on request.

References

[1] K.T. Butler, D.W. Davies, H. Cartwright, O. Isayev, A. Walsh, Machine learning for molecular and materials science, Nature 559 (7715) (2018) 547–555.
[2] R. Ramprasad, R. Batra, G. Pilania, A. Mannodi-Kanakkithodi, C. Kim, Machine learning in materials informatics: recent applications and prospects, npj Comput. Mater. 3 (1) (2017) 54.
[3] R. Tamura, K. Nagata, K. Sodeyama, K. Nakamura, T. Tokuhira, S. Shibata, T. Nakanishi, Machine learning prediction of the mechanical properties of injection-molded polypropylene through X-ray diffraction analysis, Sci. Technol. Adv. Mater. 25 (1) (2024) 2388016.
[4] O.Y. Al-Jarrah, P.D. Yoo, S. Muhaidat, G.K. Karagiannidis, K. Taha, Efficient machine learning for big data: a review, Big Data Res. 2 (3) (2015) 87–93.
[5] C. Kang, J.J.M. Machado, Y. Sekiguchi, M. Ji, C. Sato, M. Naito, A butt shear joint (BSJ) specimen for high throughput testing of adhesive bonds, J. Adhes. 99 (14) (2023) 2080–2096.
[6] C. Kang, M. Ji, Y. Sekiguchi, M. Naito, C. Sato, A high-throughput technique to evaluate the probability distribution of strength of adhesively bonded joints after moisture absorption, J. Adhes. 101 (1) (2025) 18–40.
[7] R. Potyrailo, K. Rajan, K. Stoewe, I. Takeuchi, B. Chisholm, H. Lam, Combinatorial and high-throughput screening of materials libraries: review of state of the art, ACS Comb. Sci. 13 (6) (2011) 579–633.
[8] B.C. Salzbrenner, J.M. Rodelas, J.D. Madison, B.H. Jared, L.P. Swiler, Y.L. Shen, B. L. Boyce, High-throughput stochastic tensile performance of additively manufactured stainless steel, J. Mater. Process. Technol. 241 (2017) 1–12.
[9] G.L. Hart, T. Mueller, C. Toher, S. Curtarolo, Machine learning for alloys, Nat. Rev. Mater. 6 (8) (2021) 730–755.
[10] G.X. Gu, C.T. Chen, M.J. Buehler, De novo composite design based on machine learning algorithm, Extreme Mech. Lett. 18 (2018) 19–28.
[11] C. Kim, R. Batra, L. Chen, H. Tran, R. Ramprasad, Polymer design using genetic algorithm and machine learning, Comput. Mater. Sci. 186 (2021) 110067.
[12] S. Wu, Y. Kondo, M.A. Kakimoto, B. Yang, H. Yamada, I. Kuwajima, R. Yoshida, Machine-learning-assisted discovery of polymers with high thermal conductivity using a molecular design algorithm, npj Comput. Mater. 5 (1) (2019) 66.
[13] S.W. Ghori, R. Siakeng, M. Rasheed, N. Saba, M. Jawaid, The role of advanced polymer materials in aerospace, in: Sustainable Composites for Aerospace Applications, Woodhead Publishing, 2018, pp. 19–34.
[14] M. Perez, A. Akhavan-Safar, R.J. Carbas, E.A. Marques, S. Wenig, L.F. da Silva, Loading rate and temperature interaction effects on the mode I fracture response of a ductile polyurethane adhesive used in the automotive industry, Materials 15 (24) (2022) 8948.
[15] K. Gurunathan, A.V. Murugan, R. Marimuthu, U.P. Mulik, D.P. Amalnerkar, Electrochemically synthesised conducting polymeric materials for applications towards technology in electronics, optoelectronics and energy storage devices, Mater. Chem. Phys. 61 (3) (1999) 173–191.
[16] C.M. Stafford, C. Harrison, K.L. Beers, A. Karim, E.J. Amis, M.R. VanLandingham, E.E. Simonyi, A buckling-based metrology for measuring the elastic moduli of polymeric thin films, Nat. Mater. 3 (8) (2004) 545–550.
[17] M. Ji, C. Kang, Y. Sekiguchi, M. Naito, C. Sato, Spectral collocation method for free vibration of sandwich plates containing a viscoelastic core, Compos. Struct. 337 (2024) 118024.
[18] Y. Sekiguchi, A. Hayashi, C. Sato, Analytical determination of adhesive layer deformation for adhesively bonded double cantilever beam test considering elastic–plastic deformation, J. Adhes. 96 (7) (2020) 647–664.
[19] C.A. Schuh, Nanoindentation studies of materials, Mater. Today 9 (5) (2006) 32–40.
[20] V. Lorenzo, C. Acebo, X. Ramis, À. Serra, Mechanical characterization of sol–gel epoxy-silylated hyperbranched poly (ethyleneimine) coatings by means of depth sensing indentation methods, Prog. Org. Coating 92 (2016) 16–22.
[21] P. Ghabezi, N.M. Harrison, Indentation characterization of glass/epoxy and carbon/epoxy composite samples aged in artificial salt water at elevated temperature, Polym. Test. 110 (2022) 107588.
[22] U.A. Shakil, M.R.M. Rejab, N. Sazali, S.A. Hassan, M.Y. Yahya, Q. Ma, Damage characterisation of amine-functionalized MWCNT reinforced carbon/epoxy composites under indentation loading, J. Mater. Res. Technol. 24 (2023) 6713–6729.
[23] J. Dean, J.M. Wheeler, T.W. Clyne, Use of quasi-static nanoindentation data to obtain stress–strain characteristics for metallic materials, Acta Mater. 58 (10) (2010) 3613–3623.
[24] P.V. Pavoor, A. Bellare, A. Strom, D. Yang, R.E. Cohen, Mechanical characterization of polyelectrolyte multilayers using quasi-static nanoindentation, Macromolecules 37 (13) (2004) 4865–4871.
[25] E.G. Herbert, W.C. Oliver, G.M. Pharr, Nanoindentation and the dynamic characterization of viscoelastic solids, J. Phys. Appl. Phys. 41 (7) (2008) 074021.
[26] Z. Wang, C. Wang, Y.L. Zhao, J.J. Kai, C.T. Liu, C.H. Hsueh, Fatigue studies of CoCrFeMnNi high entropy alloy films using nanoindentation dynamic mechanical analyses, Surf. Coating. Technol. 410 (2021) 126927.
[27] K. Durst, V. Maier, Dynamic nanoindentation testing for studying thermally activated processes from single to nanocrystalline metals, Curr. Opin. Solid State Mater. Sci. 19 (6) (2015) 340–353.
[28] L. Qian, H. Zhao, Nanoindentation of soft biological materials, Micromachines 9 (12) (2018) 654.
[29] N. Moharrami, S.J. Bull, A comparison of nanoindentation pile-up in bulk materials and thin films, Thin Solid Films 572 (2014) 189–199.
[30] Y. Choi, H.S. Lee, D. Kwon, Analysis of sharp-tip-indentation load–depth curve for contact area determination taking into account pile-up and sink-in effects, J. Mater. Res. 19 (11) (2004) 3307–3315.
[31] M. Troyon, L. Huang, Correction factor for contact area in nanoindentation measurements, J. Mater. Res. 20 (3) (2005) 610–617.
[32] W.G. Jiang, J.J. Su, X.Q. Feng, Effect of surface roughness on nanoindentation test of thin films, Eng. Fract. Mech. 75 (17) (2008) 4965–4972.
[33] K. Houjou, K. Shimamoto, H. Akiyama, C. Sato, Experimental investigations on the effect of a wide range of strain rates on mechanical properties of epoxy adhesives, and prediction of creep and impact strengths, J. Adhes. 98 (5) (2022) 449–463.
[34] N. Abe, Y. Sekiguchi, C. Sato, Parameter identification of material model of toughened adhesive polymer for elasto-plastic finite element analysis, J. Adhesion Soc. Japan 54 (2018) 358–366, https://doi.org/10.11618/adhesion.54.358.
[35] L.F. Da Silva, D.A. Dillard, B. Blackman, R.D. Adams (Eds.), Testing Adhesive Joints: Best Practices, John Wiley & Sons Incorporated, 2012.
[36] NF T 76-142, Methode De Preparation De Plaques Dadhesifs Structuraux Pour La Realisation Deprouvettes Dessai De Caracterisation, 1988.
[37] P. Kraisornkachit, M. Naito, C. Kang, C. Sato, Multi-objective optimization of adhesive joint strength and elastic modulus of adhesive epoxy with active learning, Materials 17 (12) (2024) 2866.
[38] S. Pathak, S.R. Kalidindi, C. Klemenz, N. Orlovskaya, Analyzing indentation stress–strain response of $LaGaO_3$ single crystals using spherical indenters, J. Eur. Ceram. Soc. 28 (11) (2008) 2213–2220.
[39] W.C. Oliver, G.M. Pharr, Measurement of hardness and elastic modulus by instrumented indentation: advances in understanding and refinements to methodology, J. Mater. Res. 19 (1) (2004) 3–20.
[40] M.L. Oyen, R.F. Cook, A practical guide for analysis of nanoindentation data, J. Mech. Behav. Biomed. Mater. 2 (4) (2009) 396–407.
[41] W.C. Oliver, G.M. Pharr, An improved technique for determining hardness and elastic modulus using load and displacement sensing indentation experiments, J. Mater. Res. 7 (6) (1992) 1564–1583.
[42] J. Hay, Introduction to instrumented indentation testing, Exp. Tech. 33 (6) (2009) 66–72.
[43] R. Lewandowski, B. Chorążyczewski, Identification of the parameters of the Kelvin–Voigt and the Maxwell fractional models, used to modeling of viscoelastic dampers, Comput. Struct. 88 (1–2) (2010) 1–17.

[44] J. Gaspar, S.F. Chen, A. Gordillo, M. Hepp, P. Ferreyra, C. Marqués, Digital lock in amplifier: study, design and development with a digital signal processor, Microprocess. Microsyst. 28 (4) (2004) 157–162.
[45] G.M. Odegard, T.S. Gates, H.M. Herring, Characterization of viscoelastic properties of polymeric materials through nanoindentation, Exp. Mech. 45 (2) (2005) 130–136.
[46] J. Hay, P. Agee, E. Herbert, Continuous stiffness measurement during instrumented indentation testing, Exp. Tech. 34 (2010) 86–94.
[47] R. Mouginot, P. Spätig, H.P. Seifert, Dynamic study of contact damping in martensitic stainless steels using nano-indentation, Mech. Mater. 149 (2020) 103541.
[48] B.N. Lucas, W.C. Oliver, J.E. Swindeman, The Dynamics of frequency-specific, depth-sensing Indentation Testing, 522, MRS Online Proceedings Library (OPL), 1998, p. 3.
[49] J.E. Jakes, C.R. Frihart, J.F. Beecher, R.J. Moon, D.S. Stone, Experimental method to account for structural compliance in nanoindentation measurements, J. Mater. Res. 23 (4) (2008) 1113–1127.
[50] C. Gao, M. Liu, Instrumented indentation of fused silica by Berkovich indenter, J. Non-Cryst. Solids 475 (2017) 151–160.
[51] M.L. Oyen, R.F. Cook, Load–displacement behavior during sharp indentation of viscous–elastic–plastic materials, J. Mater. Res. 18 (1) (2003) 139–150.